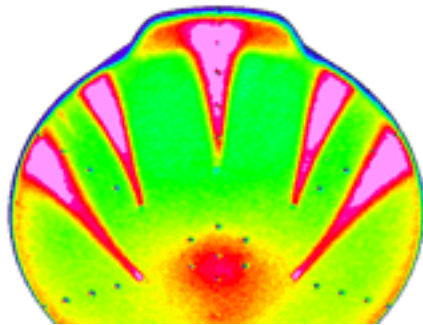




AIAA 2002-4506

Control Surface and Afterbody Experimental Aeroheating for a Proposed Mars Smart Lander Aeroshell

Derek S. Liechty, Brian R. Hollis, and Karl T. Edquist
NASA Langley Research Center
Hampton, VA



**AIAA Atmospheric Flight Mechanics
Conference and Exhibit**
August 5-8, 2002
Monterey, California

CONTROL SURFACE AND AFTERBODY EXPERIMENTAL AEROHEATING FOR A PROPOSED MARS SMART LANDER AEROSHELL

Derek S. Liechty*, Brian R. Hollis†, and Karl T. Edquist†
 NASA Langley Research Center
 Hampton, VA

ABSTRACT

Several configurations, having a Viking aeroshell heritage and providing lift-to-drag required for precision landing, have been considered for a proposed Mars Smart Lander. An experimental aeroheating investigation of two configurations, one having a blended tab and the other a blended shelf control surface, has been conducted at the NASA Langley Research Center in the 20-Inch Mach 6 Air Tunnel to assess heating levels on these control surfaces and their effects on afterbody heating. The proposed Mars Smart Lander concept is to be attached through its aeroshell to the main spacecraft bus, thereby producing cavities in the forebody heat shield upon separation prior to entry into the Martian atmosphere. The effects these cavities will have on the heating levels experienced by the control surface and the afterbody were also examined. The effects of Reynolds number, angle-of-attack, and cavity location on aeroheating levels and distributions were determined and are presented. At the highest angle-of-attack, blended tab heating was increased due to transitional reattachment of the separated shear layer. The placement of cavities downstream of the control surface greatly influenced aeroheating levels and distributions. Forebody heat shield cavities had no effect on afterbody heating and the presence of control surfaces decreased leeward afterbody heating slightly.

NOMENCLATURE

<p>h heat transfer coefficient, $h=q/(H_{aw}-H_w)$, (slug/ft²/s or kg/m²/s)</p> <p>H enthalpy (BTU/lbm or J/kg)</p> <p>L length of vehicle from nose to base (in. or m)</p> <p>M Mach number</p> <p>q surface heat transfer rate (BTU/ft²/s or W/m²)</p> <p>R model reference radius (in. or m)</p> <p>R_b model base radius (in. or m)</p> <p>R_n model nose radius (in. or m)</p> <p>R_c model corner radius (in. or m)</p> <p>Re unit Reynolds number (1/ft or 1/m)</p> <p>r radial distance from symmetry axis (in. or m)</p> <p>U velocity magnitude (ft/s or m/s)</p> <p>w cavity diameter (in. or m)</p> <p>z distance along symmetry axis from nose (in. or m)</p> <p>α angle-of-attack (deg)</p> <p>η forebody half angle (deg)</p> <p>γ ratio of specific heats</p>	<p>θ cavity orientation angle (deg)</p> <p>ρ density (slug/ft³ or kg/m³)</p> <p>ξ first afterbody cone angle (deg)</p> <p>ζ second afterbody cone angle (deg)</p> <p><u>Subscripts</u></p> <p>∞ freestream static conditions</p> <p>aw adiabatic wall conditions</p> <p>D model diameter (in. or m)</p> <p>FR conditions from Fay-Riddell calculation for a hemisphere</p> <p>fs full scale dimensions</p> <p>w conditions evaluated at the wall</p>
--	--

* Aerospace Technologist
 † Aerospace Technologist, Senior Member AIAA

Copyright © 2002 by the American Institute of Aeronautics and Astronautics, Inc. No copyright is asserted in the United States under Title 17, U.S. Code. The U.S. Government has a royalty-free license to exercise all rights under the copyright claimed herein for Governmental Purposes. All other rights are reserved by the copyright owner.

INTRODUCTION

The next generation of Mars landers¹ are being designed to enable precision landings at specific locations of particular scientific interest. The first generation entry, descent and landing systems, such as Viking and Pathfinder, achieved successful landings on Mars, but were limited in accuracy to landing sites on the order of hundreds of kilometers. The second generation landers, or smart landers, will provide scientists with the opportunity to select a particular region of interest and land within three kilometers of the intended target.

As described in Ref. 1, the baseline Mars Smart Lander (MSL) aeroshell configuration, which has no control surface, provided a low ballistic coefficient for a given vehicle mass, could provide a lift-to-drag ratio of

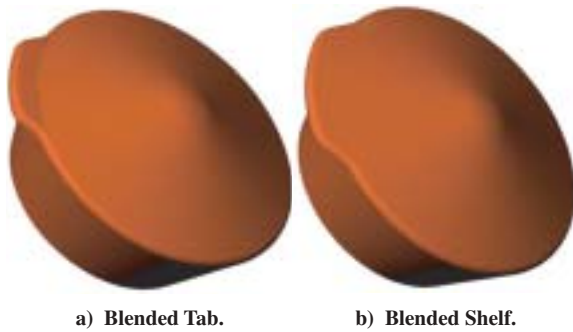


Figure 1: MSL control surface configurations.

0.18, and had significant flight heritage (e.g., Viking). However, different aeroshell configurations were considered to meet the lift-to-drag requirement of 0.22 to 0.25 in order to provide a precision landing. The baseline concept is capable of achieving these values of lift-to-drag by utilizing ballast to provide a radial center of gravity (c.g.) offset, such that the vehicle trims at an angle-of-attack. The ballast required to achieve the radial c.g. offset, however, is not insignificant.

In an attempt to save weight, tab and shelf configurations (Fig. 1) were investigated for application to the smart lander. The tab concept is inclined into the flow with respect to the forebody, while the shelf is an extension of the forebody. Tab concepts were investigated as early as 1961², and considered again for the cancelled Mars Surveyor 2001 Precision Lander mission. Both the tab and shelf concepts can be sized to achieve the required lift-to-drag ratio of 0.22-0.25 at an angle-of-attack of approximately 16-deg. The advantage of the tab concepts compared to the shelf concepts are that the tabs can be smaller, due to the higher pressure produced on the tab. A screening was performed of several tab configurations in the LaRC 20-Inch Mach 6 CF4 Tunnel to assess the aeroheating environments. From these results and computational studies^{3,4} to optimize the shape of the tab, the current blended tab configuration (Fig. 1.a) was selected. The current blended shelf configuration (Fig. 1.b) was similarly optimized^{3,4}.

The design¹ of the proposed MSL aeroshell requires that it be attached to the main spacecraft bus by way of six structural inserts which pass through holes in the forebody heat shield (Fig 2). When the aeroshell is separated from the spacecraft bus prior to entry into the Martian atmosphere, the bolts are severed and retracted, which forms cavities. The presence of these cavities in the heat shield during entry may result in high, localized heating at the downstream edge of the cavities due to flow separation and reat-

tachment within the cavities; and may be accompanied by a heating augmentation downstream of the cavities due to a change in the state of the boundary layer from laminar to transitional or turbulent. Refs. 5 and 6 discuss the effects of cavities on the proposed MSL aeroshell forebody aeroheating. The Genesis Sample Return Capsule (GSRC) also has forebody heat shield cavities. A study of the effect of forebody heat shield cavities was conducted on the GSRC, but it has a different forebody half angle than the MSL. The GSRC aeroheating environment is discussed in Ref. 7. These transitional/turbulent wedges may impact the control surfaces and result in increased heating.

The goal of the present study was to determine experimentally how the presence of forebody cavities would affect the heating levels on control surfaces and the afterbody of the proposed MSL. References 5 and 6 have shown that the cavities will have an effect on forebody heat shield aeroheating for the proposed MSL, but the impact that the cavities would have on the control surfaces and vehicle afterbody was not addressed in these references. Tests were conducted at nominal conditions of Mach 6 in air (perfect gas; $\gamma = 1.4$) with freestream Reynolds numbers from 2.1×10^6 to 5.8×10^6 per foot, resulting in Reynolds numbers based on diameter of 8.75×10^5 to 2.42×10^6 . A range of angles-of-attack from 11-deg to 20-deg was studied. The largest nominal cavity size from Ref. 5 (3.0-in. full scale diameter) was tested at the inner radial location (41% of the model radius) at various angular locations with respect to the symmetry plane. Discrete trips were placed upstream of the control surfaces to transition the flow from laminar. Windward

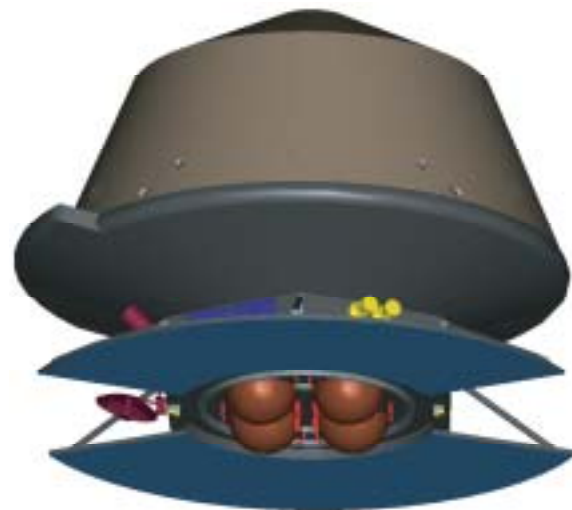


Figure 2: MSL Cruise Configuration.

afterbody heating distributions were also measured. Global heating distributions were measured using thermographic phosphors.

EXPERIMENTAL METHODS

Test Facility

Aeroheating tests were conducted in the NASA Langley 20-Inch Mach 6 Air Tunnel. This is a blow-down facility in which heated, dried and filtered air is used as the test gas. The tunnel has a two-dimensional, contoured nozzle that opens into a 20.5-in. by 20-in. test section. The tunnel is equipped with a bottom-mounted injection system that can transfer a model from the sheltered model box to the tunnel centerline in less than 0.5 seconds. Run times of up to 15 minutes are possible in this facility, although for the current aeroheating test, run times of only a few minutes were required (models are only exposed to the flow for a few seconds). The nominal reservoir conditions of this facility are stagnation pressures of 30 to 500 psia (206.8 to 3447.4 kPa) with stagnation temperatures of 760-deg to 1000-deg R (422.2 to 555.5 K), which produce perfect gas freestream flows with Mach numbers between 5.8 and 6.1 and Reynolds numbers of 0.5×10^6 to 7.3×10^6 per foot (1.64×10^6 to 23.95×10^6 per meter). A more detailed description of this facility is presented in Ref. 8.

Although the test facility does not simulate the heavier than air aspect of the Martian atmosphere, it provides the values of Re_D experienced during the hypersonic portion of the flight trajectory as well as the values of Re_θ and w/δ (transition correlations for the wind tunnel cases and for flight are presented in

Refs. 6 and 9). Figure 3 shows the values of Re_D that the proposed MSL will experience throughout the entry trajectory along with the range of values of Re_D tested in the 20-Inch Mach 6 Air Tunnel. The values tested capture the majority of the vehicle's trajectory, including the peak heating and peak dynamic pressure points. Because of the differences between the test gas and the Martian atmosphere, experimental values of Re_D which were above the values from the computed trajectory were tested in order to match values of Re_θ and w/δ in flight.

Phosphor Thermography Technique

Global surface heating distributions were calculated using the digital optical measurement method of two-color, relative-intensity, phosphor thermography¹⁰⁻¹³. Ceramic wind tunnel models are coated with a phosphor compound that fluoresces in two separate regions (green and red) of the visible light spectrum. During a wind tunnel run, the phosphor-coated model is illuminated by ultraviolet (UV) light sources, and the resulting fluorescent intensity of the model is recorded and digitized through a color CCD (charge coupled device) camera. The fluorescent intensity is dependent on both the intensity of the incident UV light and the local model surface temperature. The UV intensity dependence is removed by taking the ratio of the green to red intensity images, from which surface temperature distributions can be determined through prior calibrations. Images are acquired before the wind tunnel run and after injection of the model to the tunnel centerline during a run. Global heat transfer distributions are then computed from these temperature data using one-dimensional, constant heat-transfer coefficient conduction theory¹³.

The global phosphor thermography technique is now the standard method for aeroheating studies in Langley's hypersonic tunnels used for aerothermodynamic studies. The global data obtained using this method can be used to identify the surface heating effects of complex three-dimensional flow phenomena such as transition fronts, vortex structures, and shock interactions which are difficult to examine using conventional discrete-sensor methods such as thin-film resistance gages or coaxial surface thermocouples.

Test Model Description

In order to manufacture ceramic test models, rapid-prototype, stereolithographic (SLA) resin models were first fabricated based on surface geometry definitions in electronic data files. Wax molds of the

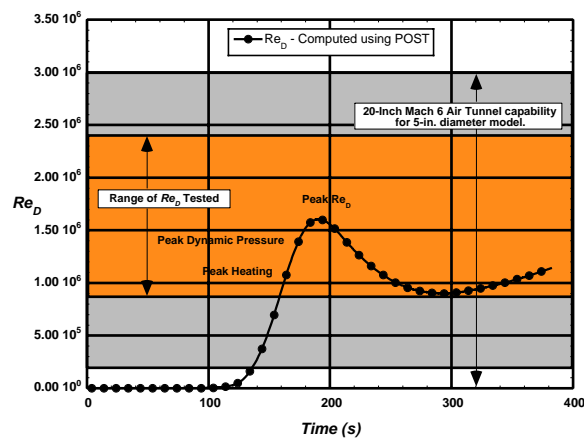


Figure 3: Values of Re_D through MSL trajectory with range of tested Re_D .

resin models were made, and then a patented¹⁴ silica ceramic slip casting technique was used to form a ceramic shell of the models. The shell was then back-filled with a hydraulically setting magnesia ceramic for strength and support. Finally, the models were coated with a mixture of phosphors suspended in a silica-based colloidal binder.

The proposed MSL entry vehicle is a 70-degree sphere-cone with a biconic afterbody (Fig. 4). Three configurations are being considered in this study. First, the baseline configuration (no control surface) was fabricated as a reference with which to compare the control surface models. The geometry of the proposed baseline MSL aeroshell is shown in Fig. 4.a and its dimensions (full scale and test model) are shown in Table 1. Next, the blended tab configuration has the same dimensions as the baseline configuration, but a control surface was added at the corner which is inclined 10-degree from the forebody heat shield. The geometry of the proposed blended tab MSL aeroshell is shown in Fig. 4.b. Finally, the blended shelf configuration, which also has the same dimensions as the baseline configuration, has a control surface added at the corner which is an extension of the 70-degree forebody half-angle. The geometry of the proposed blended shelf MSL aeroshell is shown in Fig 4.c.

The cast ceramic aeroheating models were 5-in. diameter, 0.0314-scale representations of the proposed 13.29-ft diameter Mars Smart Lander aeroshell, which were supported with a 1-in. sting mounted along the symmetry axis. Smooth models, without cavities, of each configuration were fabricated to compare with the configurations with cavities. Fig. 5 shows the three cavity configurations that were studied on the blended tab configuration (only leeward half of model is shown) and a description of these configurations is listed in Table 2. All cavities were located at $r/R = 0.41$ and had a full scale diameter of 3.0-in. The first configuration, T-5-3B, had a cavity located on the model symmetry plane with the five other cavities located at 60-degree increments around the model. The second configuration, T-5-3C, had a cavity offset 30-degree to each side of the model symmetry plane with four other cavities located at 60-degree increments around the model. The final configuration, T-5-3D, had one cavity 25-degree off the symmetry plane and another cavity located 35-degree off the symmetry plane. The forebody of the proposed MSL will have six cavities of the same size and radial location spaced at 60-degree increments, although the final size and locations have not been determined.

Small, circular marks were placed on the models to aid in data reduction and model orientation. These

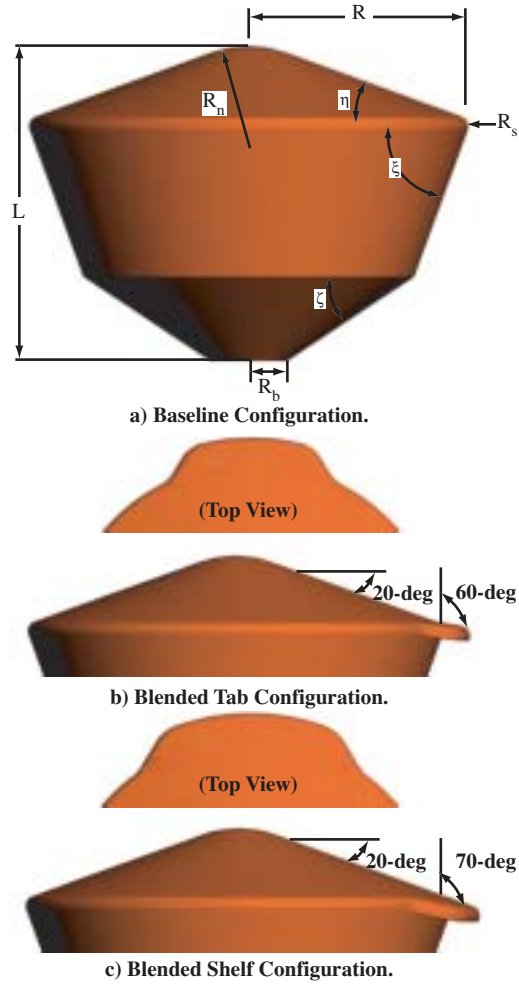


Figure 4: MSL geometries for the baseline, blended tab, and blended shelf configurations.

Parameter	Full Scale	Test Model
R (in)	79.72	2.50
R_n (in)	38.79	1.218
R_c (in)	3.89	0.122
R_b (in)	13.95	0.438
L (in)	114.52	3.596
η (deg)	20	20
ξ (deg)	70	70
ζ (deg)	33.6	33.6

Table 1: Parameters for MSL geometry.

marks, referred to as fiducial marks, do not influence the flow over the model surface. The fiducial marks can be seen in run images as dark dots and should not be confused with cavities.

Throughout this report, reference will be made to windward and leeward surfaces of the forebody. The region above the nose in the forebody images will be

Configuration	w_{fs} (in.)	Cavity Locations
T-5-3B	3.0	on symmetry plane.
T-5-3C	3.0	30-deg off symmetry plane
T-5-3D	3.0	25-deg and 35-deg off symmetry plane

Table 2: Blended tab configurations.

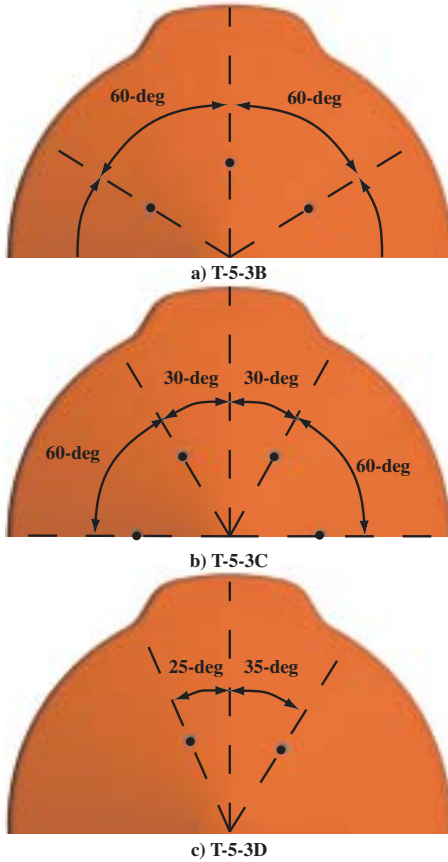


Figure 5: Blended tab cavity configurations.

Re_D	Re_∞ (1/ft)	M_∞	T_∞ (K)	ρ_∞ (kg/m ³)	U_∞ (kg/m ³)	Re_∞ (1/m)	h_{FR} (kg/m ² -s)	q_{FR} (W/cm ²)
8.75×10^5	2.1×10^6	5.95	62.0	3.35×10^{-2}	938.6	7.07×10^6	0.283	5.70
1.08×10^6	2.6×10^6	5.97	62.2	4.05×10^{-2}	943.0	8.55×10^6	0.313	6.45
1.25×10^6	3.0×10^6	5.98	62.2	4.62×10^{-2}	944.4	9.79×10^6	0.335	6.95
1.42×10^6	3.4×10^6	5.99	61.6	5.29×10^{-2}	940.1	1.13×10^7	0.356	7.25
1.71×10^6	4.1×10^6	6.00	61.3	6.41×10^{-2}	940.4	1.37×10^7	0.392	7.95
2.125×10^6	5.1×10^6	6.02	63.4	7.92×10^{-2}	958.7	1.67×10^7	0.446	9.92
2.42×10^6	5.8×10^6	6.03	62.8	8.99×10^{-2}	955.6	1.91×10^7	0.474	10.4

Table 3: Nominal flow conditions of the Langley 20-Inch Mach 6 Air Tunnel.

referred to as the leeward side of the forebody; and the region below the nose in the forebody images will be referred to as the windward side of the forebody.

Data Reduction

One-dimensional, semi-infinite solid heat conduction theory¹³ was used to compute surface heating distributions from the global surface temperature data acquired through phosphor thermography. A constant heat-transfer coefficient is assumed in this theory, and empirical corrections¹³ are made to account for changes in model substrate thermal properties with temperature. Phosphor images were acquired shortly after injection of the model to the tunnel centerline, which requires less than one second.

Data cuts were extracted from the heat transfer images. Results are presented herein in terms of a non-dimensional heat transfer coefficient ratio, h/h_{FR} , where h_{FR} is the theoretical heating computed with the Fay-Riddell¹⁵ method for a 1.2165-in. (3.09 cm) sphere, which is the radius of the spherical portion of the forebody of the test models, with a wall temperature of 300 K.

As detailed in Ref. 13, the estimated uncertainty of the phosphor thermography technique is approximately $\pm 13\%$ on the forebody and approximately $\pm 25\%$ on the afterbody.

Test Matrix and Tunnel Conditions

The data were collected at angles-of-attack of 11-deg, 16-deg and 20-deg, a side-slip angle of 0-deg, and Reynolds numbers based on model diameter of 8.75×10^5 and 2.42×10^6 . Smooth baseline, blended tab, and blended shelf configurations were tested, along with the three blended tab configurations including cavities. Both forebody and afterbody measurements were made. The nominal test conditions are listed in Table 3.

RESULTS AND DISCUSSION

Smooth Model Aeroheating and Effect of Control Surfaces

Heating images for the smooth MSL models (no cavities or discrete trips) are shown at $Re_D = 1.25 \times 10^6$ in Fig. 6 and at $Re_D = 2.42 \times 10^6$ in Fig. 7. The corresponding centerline heating ratio h/h_{FR} is plotted vs. the non-dimensional distance ratio r/R in Figs. 8 and 9, respectively.

A detailed discussion of the aeroheating characteristics of the baseline configuration MSL aeroshell can be found in Ref. 5; the following are a brief overview. The highest heating on the proposed MSL forebody, excluding the corner, did not occur at the stagnation point, which moved off of the spherical nose at the angles-of-attack studied. The highest heating stayed on the spherical nose. The rapid expansion of the inviscid flow around the corner formed a large favorable pressure gradient, which resulted in a reduction of the boundary layer thickness. This caused increased heating levels near the corner. The edge

Mach number of the baseline configuration never exceeded 1.0, except at the corner.

The presence of the blended shelf had little effect on the centerline heating distribution. The only effect it had was to increase the running length compared to the baseline model. The increase in heating attributed to the expansion of the flow around the corner of the baseline configuration is simply moved outboard to the corner of the blended shelf.

The blended tab, which was offset 10-deg into the flow from the forebody, produced a compression surface, which created a separation region upstream of the hinge-line and increased the heating levels on the surface of the blended tab. At the lowest Reynolds number ($Re_D = 1.25 \times 10^6$; Fig. 8), the size of the separation region increased with angle of attack. The heating ratio on the blended tab increased with angle-of-attack, which may at first be counter-intuitive since the blended tab became more oblique to the freestream flow because it was on the leeward surface. However, since the size of the separation region was increasing with angle-of-attack, it was more likely to reattach in a transitional state, thereby increasing the

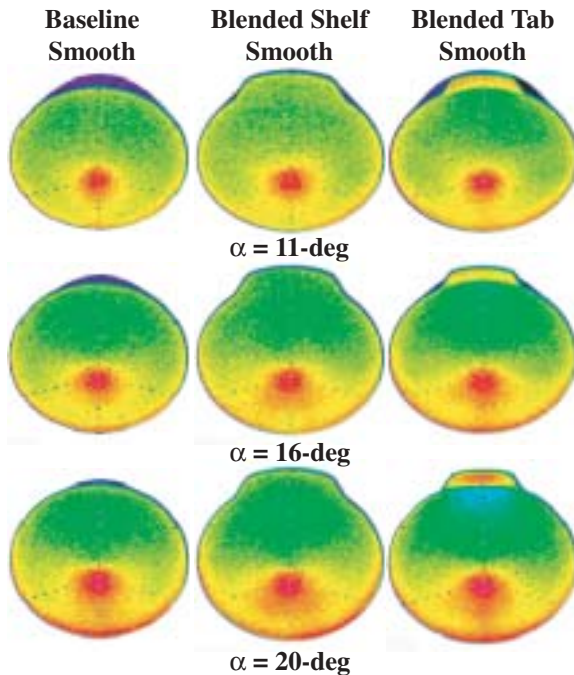


Figure 6: Smooth model global heating images at $Re_D = 1.25 \times 10^6$.

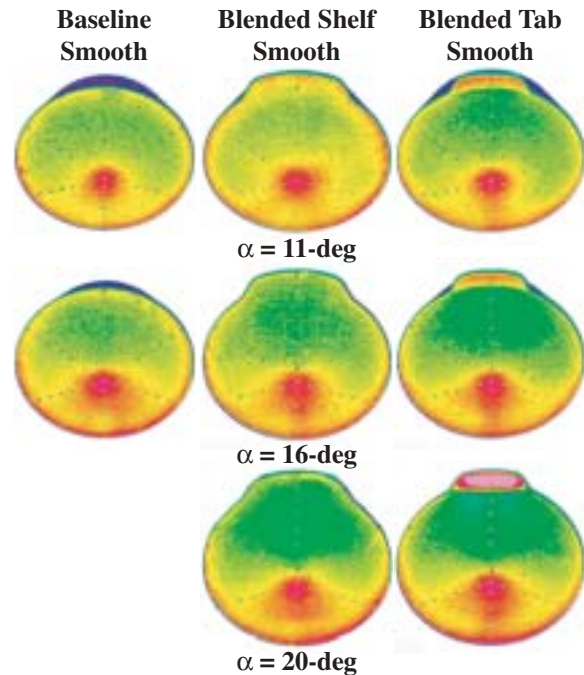


Figure 7: Smooth model global heating images at $Re_D = 2.42 \times 10^6$.



heating ratio. At the highest Reynolds number ($Re_D = 2.42 \times 10^6$; Fig. 9), the size of the separation region upstream of the blended tab decreased compared to the $Re_D = 1.25 \times 10^6$ cases (Fig. 8). The trend of increasing heating rates on the blended tab as angle-of-attack was increased was augmented for the $\alpha = 20$ -deg case at the higher Reynolds number. The transitional reattachment at this angle-of-attack increased the heating ratio on the blended tab by approximately 160%.

Effect of Cavities and Discrete Trips on Control Surface Heating

Previous studies^{5,6} have shown that the cavities located on the leeward side of the forebody of the proposed MSL are more likely to cause boundary layer transition than those on the windward side. Because of this, the effects of cavity placement on blended tab heating were studied at varying angles-of-attack and Reynolds numbers.

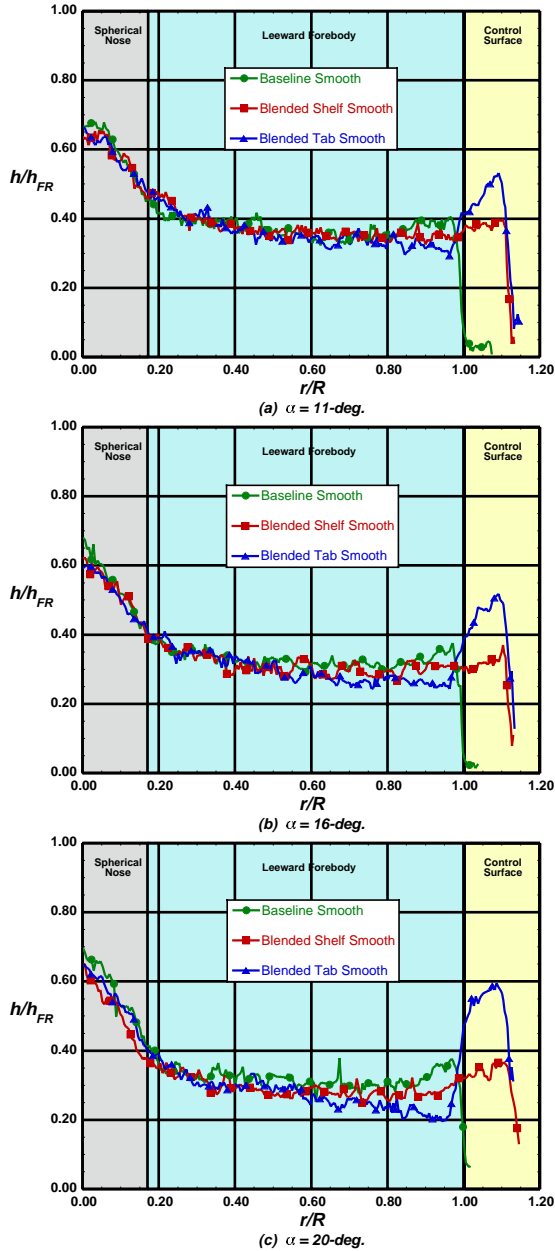


Figure 8: Effect of α on smooth model leeward centerline heating distributions at $Re_D = 1.25 \times 10^6$.

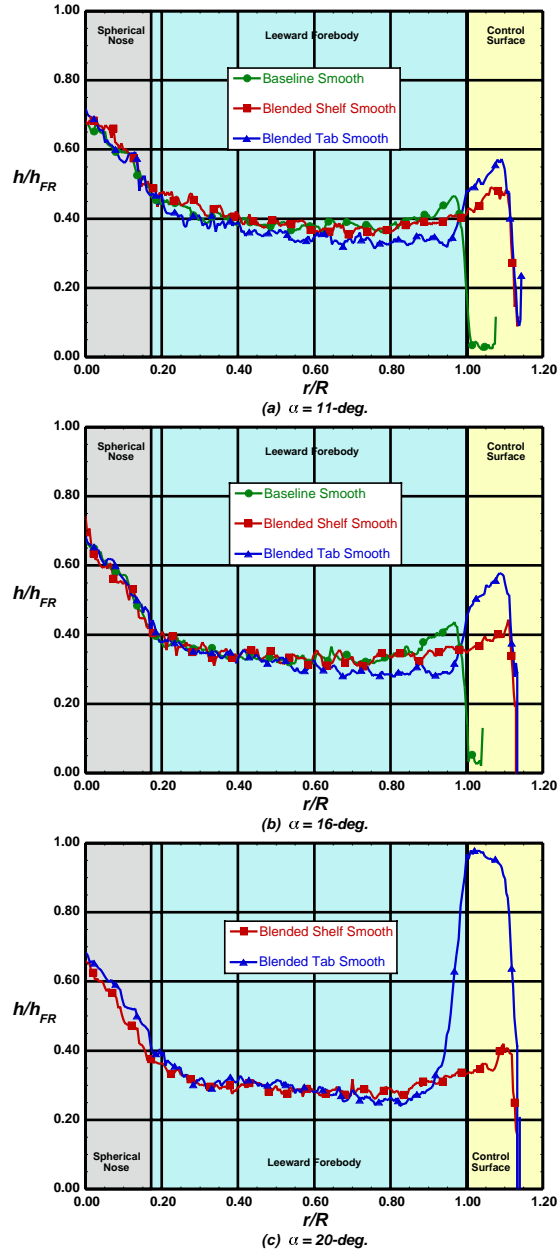


Figure 9: Effect of α on smooth model leeward centerline heating distributions at $Re_D = 2.42 \times 10^6$.

The cavities that influence heating levels on the blended tab must first be identified. Figures 10 and 11 show model configurations T-5-3B and T-5-3C, respectively, at $\alpha = 16$ -deg and 20-deg and $Re_D = 1.08 \times 10^6$, 1.42×10^6 , and 1.71×10^6 . Figure 12 shows model T-5-3D at $\alpha = 20$ -deg and $Re_D = 2.125 \times 10^6$ and 2.42×10^6 . The cavities located 60-deg (Fig. 10) or more off the leeward centerline did not effect the heating rates on the blended tab at either angle-of-attack tested, while those offset 30-deg from the centerline (Fig. 11) did at $\alpha = 16$ -deg at the highest Reynolds number. The cavities offset 25-deg and 35-deg off of the leeward centerline (Fig. 12, left and right cavities, respectively) did impact the blended tab at $\alpha = 20$ -deg.

At $\alpha = 16$ -deg, the leeward centerline cavity (Fig. 10) and the cavities located 30-deg off centerline (Fig. 11) had an effect on local aeroheating for the blended tab for the Reynolds numbers tested. However, at $\alpha = 20$ -deg (right columns in Figs. 10 and 11), by the time the cavities became effective, the separated shear layer in front of the tab was already transitional, so the heating on the blended tab was already elevated.

It is recommended that the cavities be placed 30-deg off of the leeward centerline and then at 60-deg intervals around the forebody, as configuration T-5-3C (Fig. 11) demonstrates. This is suggested because the cavity on the leeward centerline is more effective than those placed 30-deg off of the center-

line, causing higher heating for a given Reynolds number.

The effect a cavity on the leeward centerline had on blended tab heating rates and distributions will now be examined. These data for a cavity will be compared to data without cavities but with discrete trips placed near the leeward sphere-cone juncture ($r/R = 0.15$) of the model and also at 38% of the model radius. The results with discrete trips are included to provide baseline turbulent cases for comparison to the transition results corresponding to the presence of the cavity.

Global heating distributions for a range of Reynolds numbers are shown in Fig. 13 at $\alpha = 16$ -deg and in Fig. 14 at $\alpha = 20$ -deg. Corresponding leeward centerline data are plotted in Figs. 15 and 16, respectively. As the Reynolds number was increased (Figs. 15 and 16), the heating ratio downstream of the cavities and discrete trips increased. The discrete trip placed at 15% of the model radius caused the flow to transition immediately. As described in Ref. 16, there is a transition peak some distance downstream of transition onset. The transition peak is often identified with the end of transition and therefore the establishment of fully turbulent flow. It was shown, however, that the point of fully turbulent flow lies some distance downstream of the measured transitional peak. This transition peak can be easily identified in Fig. 15.c. The heating ratios for the $r/R = 0.15$ discrete trip

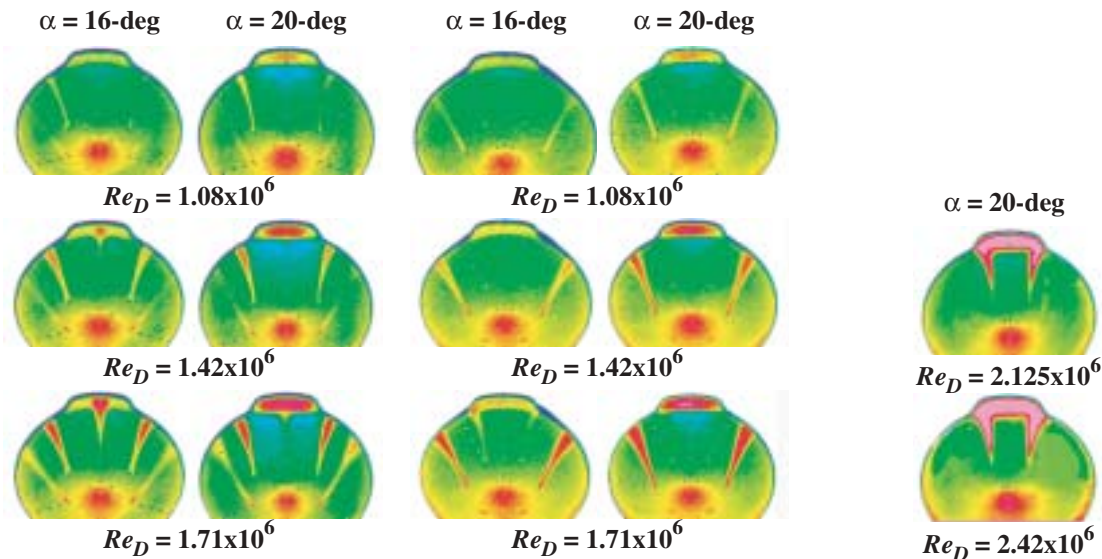


Figure 10: Effect of Re_D and α on T-5-3B.

Figure 11: Effect of Re_D and α on T-5-3C.

Figure 12: Effect of Re_D on T-5-3D.



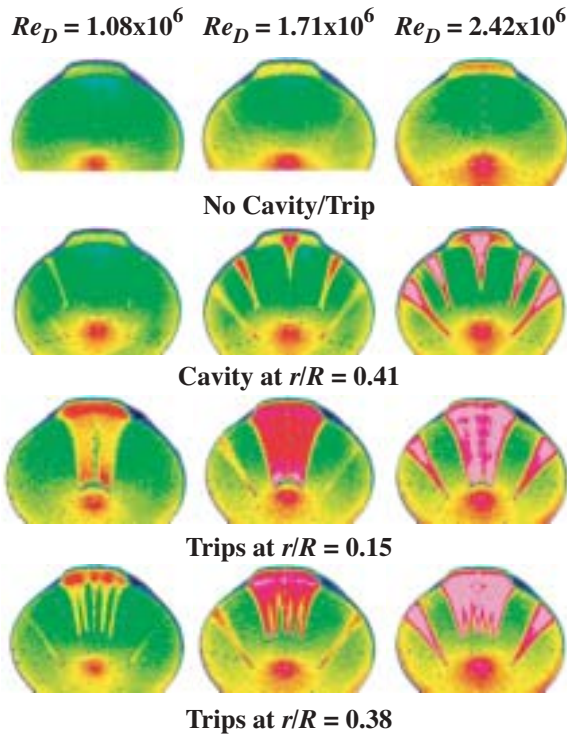


Figure 13: Effect of cavities and discrete trips on leeward side of blended tab configuration at $\alpha = 16$ -deg.

can all be seen to reach what will be referred to as the fully turbulent level for each α/Re_D combination.

The discrete trip placed at 38% of the model radius (Fig. 15) caused a much longer transition length than that of the 15% trip. In fact, at the two lowest Reynolds numbers (Figs. 15.a and 15.b), a definite transitional peak is never actually reached. For the highest Reynolds number (Fig. 15.c), the transitional peak is reached, but the heating ratio remains at this level for the remainder of the running length to the tab.

The cavity located at $r/R = 0.41$ behaves much like the discrete trip at 38% of the radius, but its transition length is greater than that of the discrete trip (Fig. 15). At the lowest Reynolds number (Figs. 15.a and 16.a), the cavity has no effect on the heating ratio compared to the smooth blended tab on the forebody of the model. The $\alpha = 20$ -deg blended tab heating, however, did increase slightly.

For fully turbulent flow upstream of the blended tab (Figs. 15 and 16; blue triangles), there did not appear to be a significant difference in blended tab heating ratio levels between $\alpha = 16$ -deg and 20-deg.

For the $\alpha = 16$ -deg data (Fig. 15), the tripped blended tab heating distributions were approximately

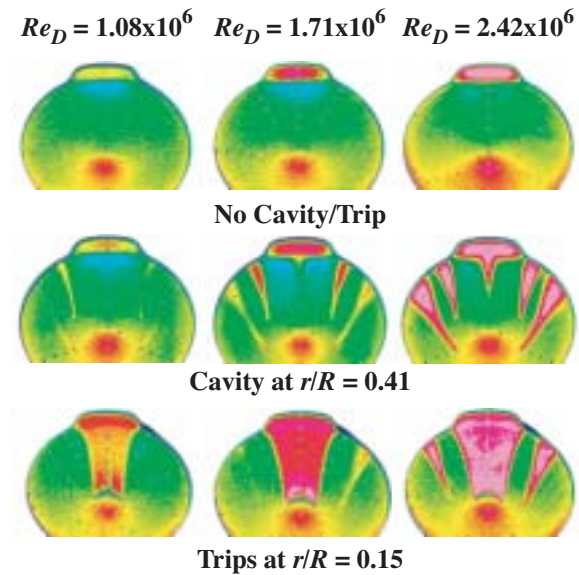
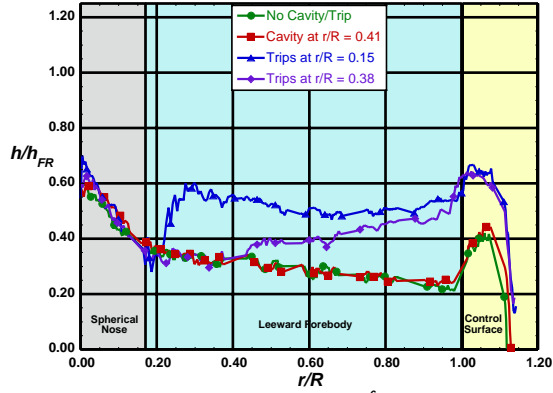


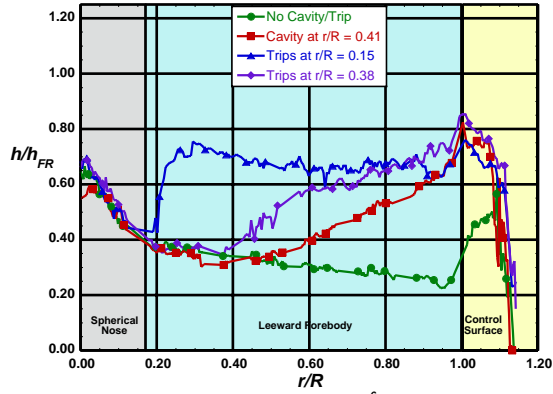
Figure 14: Effect of cavities and discrete trips on leeward side of blended tab configuration at $\alpha = 20$ -deg.

50% higher than the laminar blended tab heating distributions over the Reynolds number range tested. At $\alpha = 20$ -deg however (Fig. 16), the separated shear layer for the smooth blended tab configuration becomes transitional/turbulent, especially at the higher Reynolds numbers tested (Fig. 16.c). The smooth blended tab model heating was actually higher than those from the tripped blended tab model. This elevation in untripped downstream boundary layer heating rates on control surfaces has been observed for X-33 body flap heating¹⁷ and is believed to be due to the tripped boundary layer approaching the deflected surface resulting in a smaller separation region, a thicker shear layer attaching sooner, and lower turbulent reattachment heating levels. The laminar separation yields flow reattachment that is transitional and heating that is characteristically higher than turbulent results.

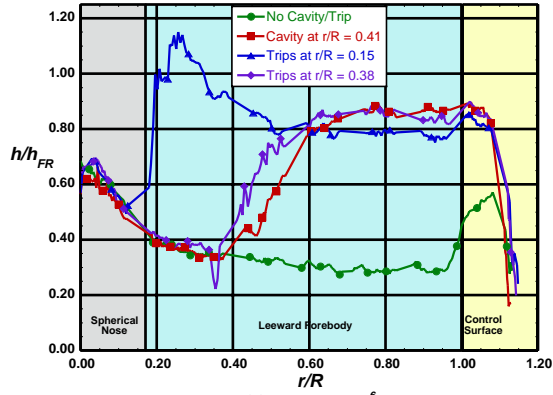
The resulting heating distribution from the cavity located at $r/R = 0.41$ appears to be bounded by the heating levels resulting from the smooth blended tab model and the blended tab with trips located at $r/R = 0.38$ at $\alpha = 16$ -deg (Fig. 15). In fact, at the highest Reynolds number (Fig. 15.c), the cavity produced higher heating levels than the $r/R = 0.15$ discrete trips,



(a) $Re_D = 1.08 \times 10^6$



(b) $Re_D = 1.71 \times 10^6$

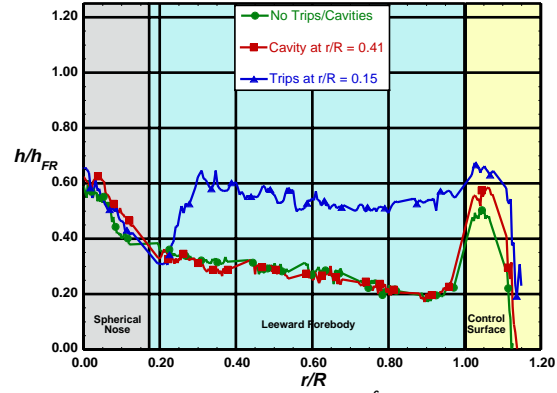


(c) $Re_D = 2.42 \times 10^6$

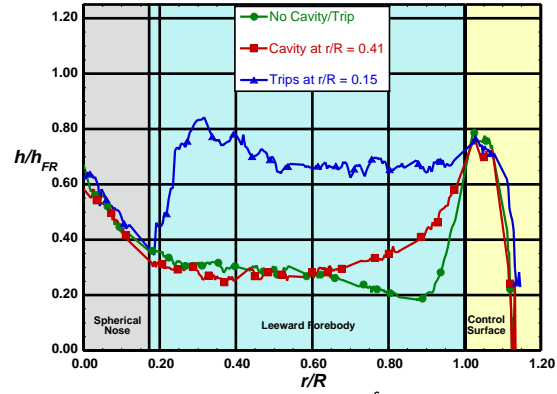
Figure 15: Leeward centerline effect of cavities and discrete trips on blended tab configuration at $\alpha = 16$ -deg.

similar to the discrete trips located at $r/R = 0.38$. For the $\alpha = 20$ -deg cases (Fig. 16), the cavity located at $r/R = 0.41$ again resulted in higher heating levels than the $r/R = 0.15$ trips at the highest Reynolds number.

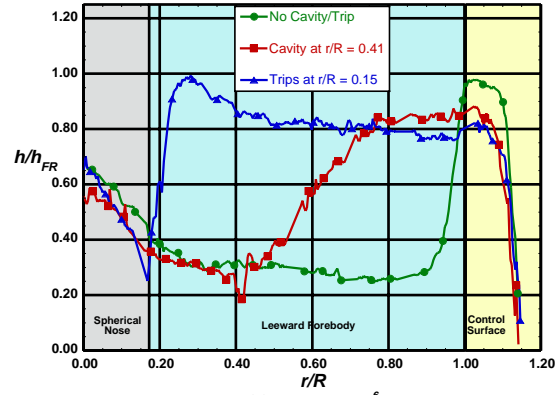
Turbulent computations have been performed⁶ on the proposed baseline MSL configuration (without a control surface) for which the location at which transition began and transition length were varied. A comparison of these computational and corresponding experimental results are shown along the leeward



(a) $Re_D = 1.08 \times 10^6$



(b) $Re_D = 1.71 \times 10^6$



(c) $Re_D = 2.42 \times 10^6$

Figure 16: Leeward centerline effect of cavities and discrete trips on blended tab configuration at $\alpha = 20$ -deg.

symmetry plane in Fig. 17 at $Re_D = 2.42 \times 10^6$ for $\alpha = 16$ -deg. Because boundary layer transition in the experiment was produced by cavities and discrete trips as opposed to occurring naturally, transition in the computations was modeled in several different ways in order to attempt to model the data. Computations were performed with: the boundary layer fully turbulent over the length of the vehicle; natural transition beginning at the location of the cavity; and

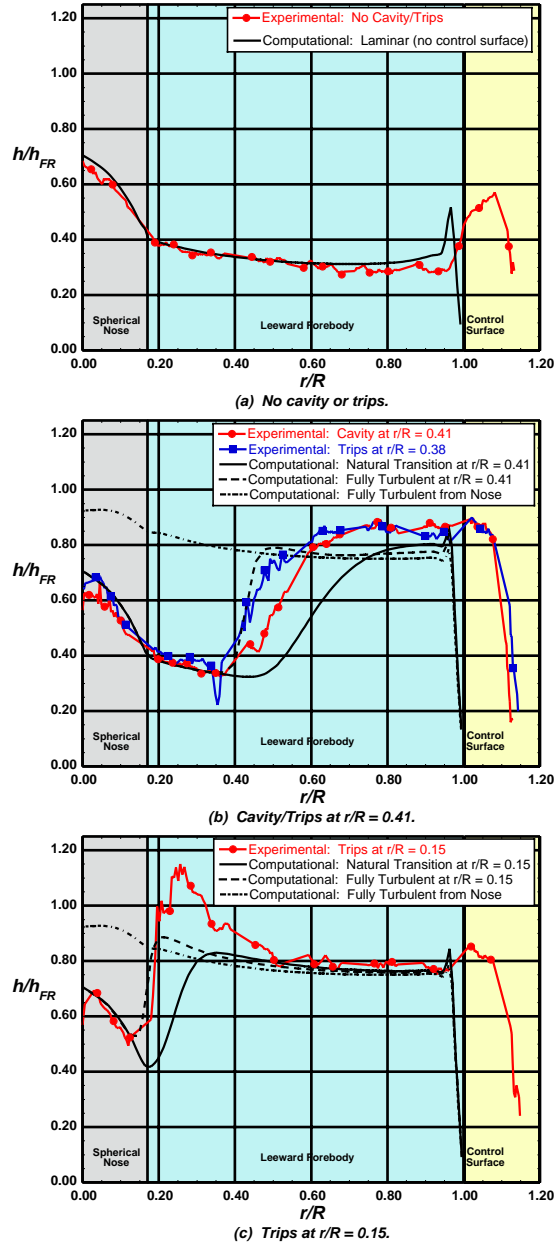


Figure 17: Comparison of experimental and computational laminar and tripped flow at $Re_D = 2.42 \times 10^6$, $\alpha = 16$ -deg.

zero-length transition to fully-turbulent flow at the cavity location. For the natural transition computations, the transition length was set equal to the running length of the flow from the nose to the cavity.

Figure 17.a is a comparison of the laminar solution without a control surface to the corresponding non-tripped experimental case. The agreement is well within the $\pm 13\%$ uncertainty from the nose up to the corner. The effects of the separation region can be seen just upstream of the blended tab where the exper-

imental heating is lower than the computed heating for the baseline configuration.

Figure 17.b is a comparison of experiment and computations where the flow is tripped at approximately $r/R = 0.41$. The experimental results shown include both a cavity at $r/R = 0.41$ and discrete trips at $r/R = 0.38$. Computational results include natural transition length and zero-length transition starting at $r/R = 0.41$ and fully turbulent flow from the nose. The heating levels computed by assuming fully turbulent flow beginning at the cavity location (i.e. zero-length transition) were higher than those computed when the flow was treated as fully turbulent from the nose of the vehicle. As described in Ref. 6, this difference was attributed to the fact the boundary layer thickness at a given location was greater for the fully turbulent flow from the nose because of the longer running length over which the turbulent boundary layer had to grow. The $r/R = 0.41$ tripped flow has a thinner boundary layer, therefore higher heating. For both the cavity and discrete trip data, the peak values were higher than either the natural or zero-length transition computations by more than 15% to 20%, which was outside the experimental uncertainty. The present method for predicting turbulent heating levels did not include the actual heat-shield cavities in the computational geometry, and their possible effects on the flow field (i.e. circulation within the cavity, shocks at the lip of the cavity, boundary layer separation and vortex formation downstream of the cavity) may be a cause for the differences seen between prediction and experiment. Also, the flow may not have reached fully turbulent heating. It may still be experiencing the transitional peak discussed earlier.

Figure 17.c is a comparison of experiment and computations where the flow is tripped at approximately $r/R = 0.15$. Discrete trips were used to trip the flow in the experiment. Again, the computations included are for natural and zero-length transition at $r/R = 0.15$ and fully turbulent flow from the nose. The fully turbulent from the nose computations are slightly lower than the zero-length transition from the discrete trip, which was slightly lower than the natural transition computation. The initial peak in the experimental data was approximately 25% higher than the predicted initial peak (zero-length transition), but the experimental and computational results come to within 5% of each other downstream of transition, indicating that the fully turbulent level has been reached. For a more in-depth comparison of experimental and computational results for the MSL, see Ref. 6.

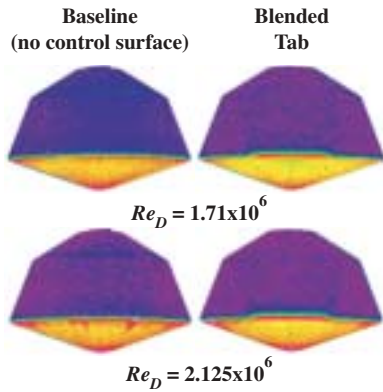


Figure 18: Leeward Afterbody for baseline (left) and blended tab (right) configurations at $\alpha = 11$ -deg.

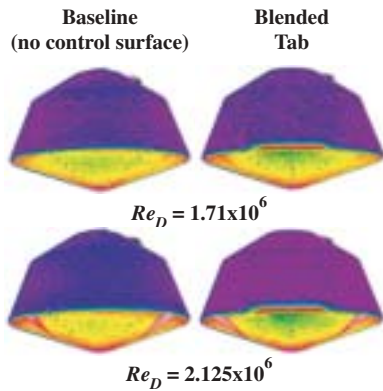


Figure 19: Leeward Afterbody for baseline (left) and blended tab (right) configurations at $\alpha = 16$ -deg.

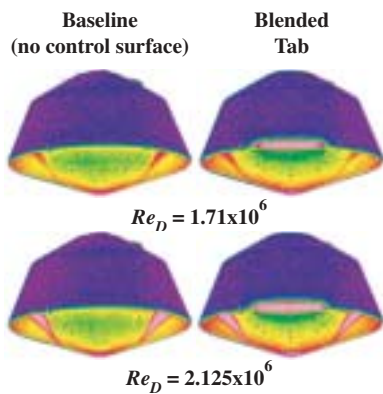


Figure 20: Leeward Afterbody for baseline (left) and blended tab (right) configurations at $\alpha = 20$ -deg.

Effect of Cavities and Control Surfaces on Leeward Afterbody Heating

Leeward afterbody heating images for both the baseline and blended tab configurations are shown in Figs. 18, 19 and 20 for angles-of-attack of 11-deg, 16-deg and 20-deg, respectively, for which the color scale has been decreased from a maximum of $h/h_{FR} = 0.8$ to $h/h_{FR} = 0.5$. The corresponding centerline non-dimensional heating data are shown in Figs. 21, 22 and 23, respectively. Heating data are plotted vs. the non-dimensional distance z/R , where $z/R = 0.38$ is the location of the corner of the baseline configuration. The uncertainty in this data is approximately $\pm 25\%$ because of the much smaller increase in surface temperature than that of the forebody during the run. This is the reason for the large amount of scatter in the data at the scale shown. All heating ratios are below $h/h_{FR} = 0.05$, which are significantly lower than those of the forebody. There is also a slight difference between the afterbody heating for the baseline configuration compared to the blended tab configuration. The blended tab configuration heating levels are gen-

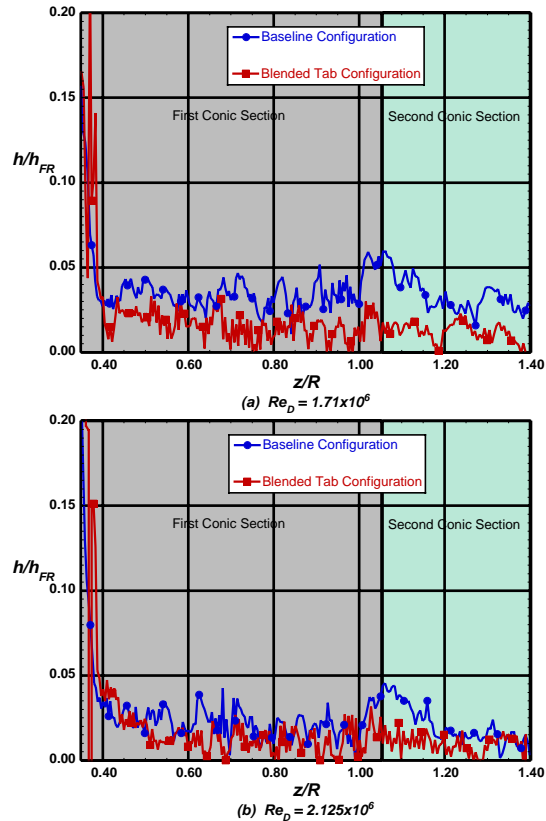
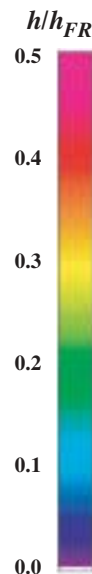


Figure 21: Leeward afterbody centerline heating at $\alpha = 11$ -deg.

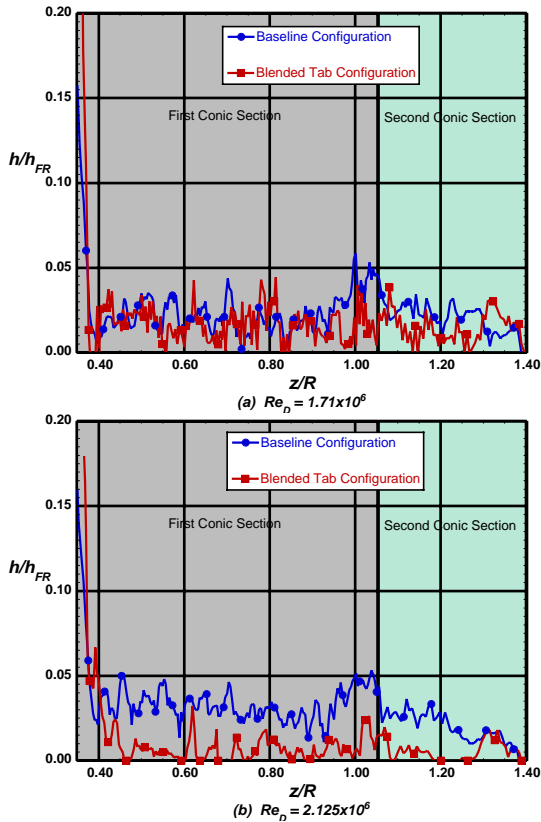


Figure 22: Leeward afterbody centerline heating at $\alpha = 16$ -deg.

erally lower than those of the baseline configuration, especially at $\alpha = 11$ -deg and 16 -deg.

In Figs. 19 and 20, the forebody cavities have tripped the boundary layer. When the transitional/turbulent wedges reach the corner of the vehicle, the boundary layer relaminarizes due to the strong negative pressure gradient. Thus the cavities have no effect on leeward afterbody heating.

Windward Afterbody Heating

Windward afterbody global heating images are shown in Fig. 24 and the corresponding centerline heating distributions are shown in Fig. 25. Heating data are plotted vs. the non-dimensional distance z/R . Once again, the temperature rise during a run is small compared to that of the forebody, so the error is approximately $\pm 25\%$. As angle-of-attack was increased from 11 -deg to 20 -deg, the heating ratio on the windward centerline increased. An increase in heating was also seen as Reynolds number increased, especially at $\alpha = 20$ -deg. A comparison to computations is included for the $\alpha = 20$ -deg case in Fig. 25.c. Good agreement (well within the $\pm 25\%$ uncertainty) between prediction and experiment was achieved.

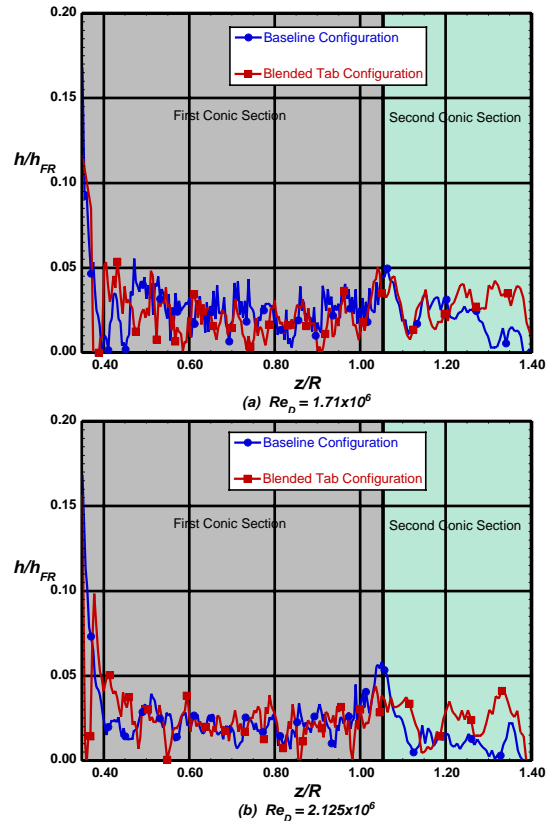


Figure 23: Leeward afterbody centerline heating at $\alpha = 20$ -deg.

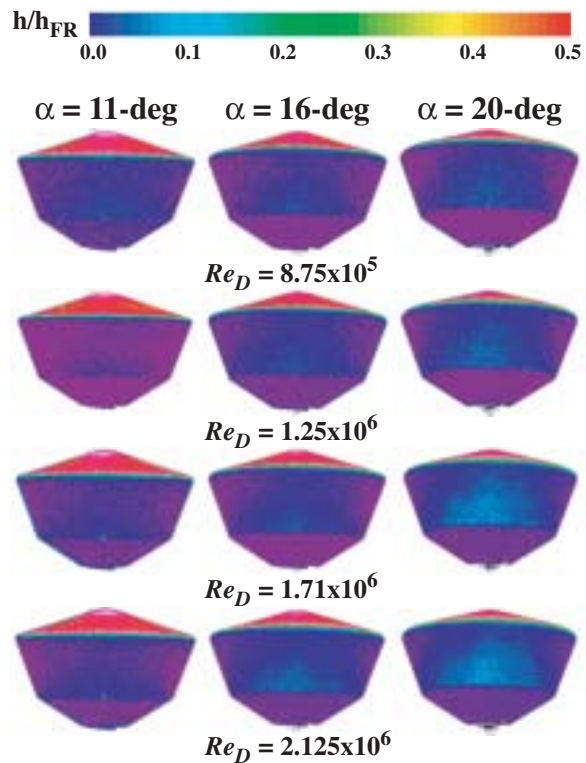


Figure 24: Windward afterbody global heating.

SUMMARY AND CONCLUSIONS

An experimental aeroheating study was conducted on the proposed Mars Smart Lander aeroshell in the NASA Langley 20-Inch Mach 6 Air Tunnel using the technique of phosphor thermography. This test was conducted in order to determine the aeroheating characteristics for several control surface configurations (the blended shelf and blended tab) and to determine the effects forebody cavities had on control surface heating distributions and levels. The afterbody heating was also examined to determine what, if any, impact the cavities and control surfaces had on heating.

The presence of the blended shelf had little effect on the proposed MSL aeroshell forebody heating. The only effect it had was to increase the running length compared to the baseline model (no control surface). The blended tab, which is offset 10-deg into the flow from the forebody, produced a compression surface, which created a separation region upstream of the hinge-line and increased the heating levels on the surface of the blended tab. At the highest value of Reynolds number tested and 20-deg angle-of-attack, the separated shear layer reattached transitionally, causing heating rates greater than those at the nose of the vehicle.

The cavity locations that influence heating levels on the blended tab were identified for a radial location of 41% of the model radius. It was found that cavities offset 60-deg or more off of the leeward centerline do not impact blended tab heating for the angles-of-attack studied; but, cavities up to at least 35-deg off of the leeward centerline do.

Blended tab heating ratios were studied for several cavity and discrete trip configurations. Discrete trips located at 15% of the model radius caused the boundary layer to transition immediately, resulting in a transition peak in the heating ratio, followed by fully turbulent heating. Discrete trips located at 38% of the model radius resulted in a longer transition length. For the lowest Reynolds numbers, a definite transition peak was never reached. For the highest Reynolds number, the transition peak is reached, but the fully turbulent heating level is never reached. The cavity located at 41% of the model radius behaves much like the discrete trip located at 38% of the model radius, but its transition length is greater than that of the discrete trip. For the cases where the boundary layer was tripped downstream of the blended tab, heating was generally higher than for the untripped cases. The exception being at an angle-of-attack of 20-deg for the highest Reynolds number, where the smooth configuration resulted in higher tab heating levels due to the

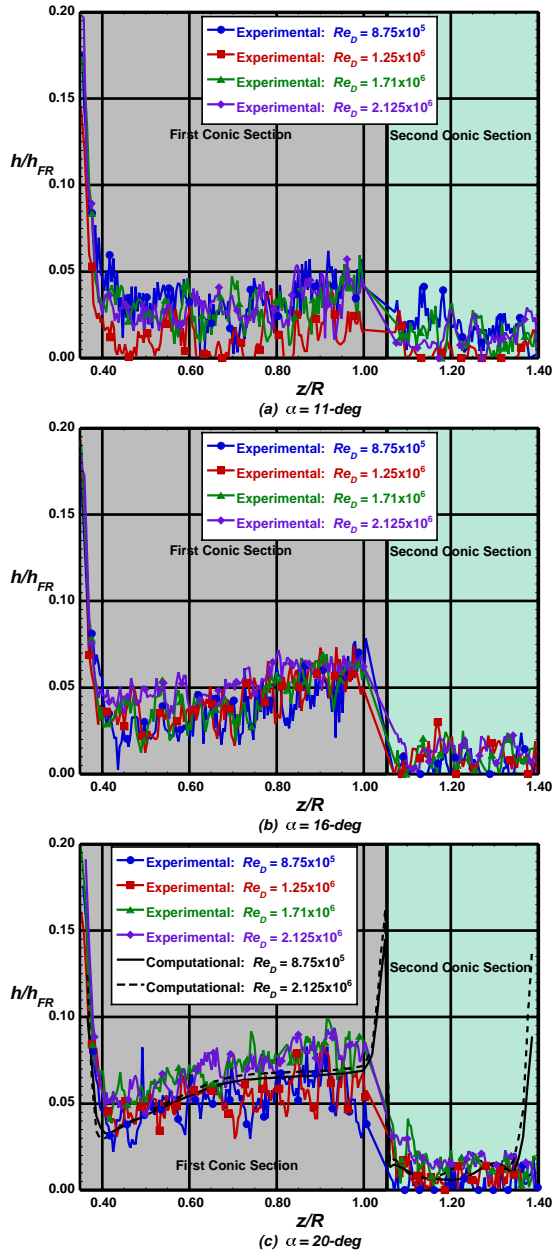


Figure 25: Windward afterbody centerline heating distribution.

transitional reattachment heating levels being higher than the turbulent levels.

Afterbody heating levels were examined to determine the effects of the presence of the cavities and control surfaces. It was found that the forebody cavities had negligible effects on afterbody heating; and control surfaces decreased leeward afterbody heating slightly.

ACKNOWLEDGEMENTS

The authors would like to acknowledge the contributions of the following individuals to this research: Jonny Ellis, Grace Gleason, and Roland Hatten for operation of the 20-Inch Mach 6 Air Tunnel and data acquisition support; Joe Powers and Mark Griffith for fabrication of the ceramic models; Kathy Kuykendoll for model fidelity measurements and fiducial mark placement; Mary Kae Lockwood for programmatic support; and Mark McMillin for providing the CAD files necessary to fabricate the models.

REFERENCES

- ¹Lockwood, M.K., Powell, R.W., Graves, C.A., Carman, G.L., "Entry System Design Considerations for Mars Landers," American Astronautical Society Paper 01-023, January/February 2001.
- ²Sammonds, R.I., Dickey, R.R., "Effectiveness of Several Control Arrangements on a Mercury-Type Capsule," NASA TM X-579, October, 1961.
- ³Prabhu, R.K., "Inviscid Flow Computations of Several Aeroshell Configurations for a '07 Mars Lander," NASA CR-2001-210851, April 2001.
- ⁴Prabhu, R.K., "Inviscid Flow Computations of Two '07 Mars Lander Aeroshell Configurations Over a Mach Number Range of 2 to 24," NASA CR-2001-210852, April 2001.
- ⁵Liechty, D.S., Hollis, B.R., "Heat Shield Cavity Parametric Experimental Aeroheating for a Proposed Mars Smart Lander Aeroshell," AIAA Paper 2002-2746, June 2002.
- ⁶Hollis, B.R., Liechty, D.S., "Boundary Layer Transition Correlations and Aeroheating Predictions for Mars Smart Lander," AIAA Paper 2002-2745, June 2002.
- ⁷Cheatwood, F.M., Merski, N.R., Riley, C.J., Mitcheltree, R.A., "Aerothermodynamic Environment Definition for the Genesis Sample Return Capsule," AIAA Paper 2001-2889, June 2001.
- ⁸Micol, J.R., "Hypersonic Aerodynamic/Aerothermodynamic Testing Capabilities at Langley Research Center: Aerothermodynamic Facilities Complex," AIAA Paper 95-2107, June 1995.
- ⁹Edquist, K. and Loomis, M., "Aeroheating Environments for Mars Smart Lander Configurations," AIAA Paper 2002-4505, August 2002.
- ¹⁰Buck, G.M., "Automated Thermal Mapping Techniques Using Chromatic Image Analysis," NASA TM 101554, April 1989.
- ¹¹Buck, G.M., "Surface Temperature/Heat Transfer Measurement Using a Quantitative Phosphor Thermography System," AIAA Paper 91-0064, January 1991.
- ¹²Merski, N.R., "A Relative-Intensity, Two-Color Phosphor Thermography System," NASA TM 104123, September 1991.
- ¹³Merski, N.R., "Reduction and Analysis of Phosphor Thermography Data with the IHEAT Software Package," AIAA Paper 98-0712, January 1998.
- ¹⁴Buck, G.M., and Vasques, P., "An Investment Ceramic Slip-Casting Technique for Net-Form, Precision, Detailed Casting of Ceramic Models," U.S. Patent 5,266,252, November 1993.
- ¹⁵Fay, J.A., and Riddell, F.R., "Theory of Stagnation Point Heat Transfer in Dissociated Air," *Journal of Aeronautical Sciences*, Vol 25, No. 2, 1958, pp. 73-85.
- ¹⁶Horvath, T.J., Berry, S.A., Hollis, B.R., Chang, C., Singer, B.A., "Boundary Layer Transition On Slender Cones In Conventional And Low Disturbance Mach 6 Wind Tunnels," AIAA Paper 2002-2743, June 2002.
- ¹⁷Horvath, T.J., Berry, S.A., Hollis, B.R., Liechty, D.S., Hamilton, H.H. and Merski, N.R., "X-33 Experimental Aeroheating at Mach 6 Using Phosphor Thermography," AIAA Paper 99-3558, June/July 1999.